

The critical role of shell in enhanced fluorescence of metal-dielectric core-shell nanoparticles

Song Sun,^{*,†,‡,||} Ilia L. Rasskazov,^{*,¶,||} P. Scott Carney,[¶] Taiping Zhang,^{†,‡} and Alexander Moroz^{*,§}

[†]*Microsystem and Terahertz Research Center, China Academy of Engineering Physics, No. 596, Yinhe Road, Shuangliu, Chengdu, 610200, China*

[‡]*Institute of Electronic Engineering, China Academy of Engineering Physics, Mianyang, 621999, China*

[¶]*The Institute of Optics, University of Rochester, Rochester, NY 14627, USA*

[§]*Wave-scattering.com*

^{||}*Contributed equally to this work*

E-mail: sunsong@mtrc.ac.cn; irasskaz@ur.rochester.edu; wavescattering@yahoo.com

Abstract

Large scale simulations are performed by means of the transfer-matrix method to reveal optimal conditions for metal-dielectric core-shell particles to induce the largest fluorescence on their surfaces. With commonly used plasmonic cores (Au and Ag) and dielectric shells (SiO₂, Al₂O₃, ZnO), optimal core and shell radii are determined to reach maximum fluorescence enhancement for each wavelength within 550–850 nm (Au core) and 390–500 nm (Ag core) bands, in both air and aqueous hosts. The peak value of the maximum achievable fluorescence enhancement factors of core-shell nanoparticles, taken over entire wavelength interval, increases with the shell refractive index and can reach values up to 9 and 70 for Au and Ag cores, within 600 – 700 nm

and 400 – 450 nm wavelength ranges, respectively, which is much larger than that for corresponding homogeneous metal nanoparticles. Replacing air by an aqueous host has a dramatic effect of nearly halving the sizes of optimal core-shell configurations at the peak value of the maximum achievable fluorescence. In the case of Au cores, the fluorescence enhancements for wavelengths within the first near-infrared biological window (NIR-I) between 700 and 900 nm can be improved twofold compared to homogeneous Au particle when the shell refractive index $n_s \gtrsim 2$. As a rule of thumb, the wavelength region of optimal fluorescence (maximal nonradiative decay) turns out to be red-shifted (blue-shifted) by as much as 50 nm relative to the localized surface plasmon resonance wavelength of corresponding optimized core-shell particle. Our results provide important design rules and general guidelines for enabling versatile platforms for imaging, light source, and biological applications.

1 Introduction

Fluorescence-based spectroscopy and imaging techniques have become a promising solution to meet the demands of various emerging applications such as single molecule detection,^{1,2} early diagnosis,^{3–5} food and drug safety.⁶ The advantage of fluorescence emitters to label the target species at a molecular level makes it an ideal tool for fingerprint tags.⁷ Fluorescence spontaneous emission also serves as the foundation of advanced light sources such as micro/nano light emitting diodes (LEDs) for high-resolution displays^{8,9} and single photon sources for quantum photonics.^{10,11} Independent spatial and temporal radiation characteristics of fluorescence emitters have been employed in a super-resolution imaging. Despite all those attractive features, intrinsic fluorescence emission is very weak, and challenges the development of high performance devices.

Plasmonic nanostructures hold a great potential in enhancing fluorescence emission.^{12–16} On one hand, collective electron oscillations on the surface of plasmonic nanostructure can generate a strong local electric field enhancement to boost the excitation rate of the flu-

orescence emitter.^{12,13,17–19} On the other hand, the presence of metal nanostructure in the vicinity of the fluorescence emitter affects the local density of optical states (LDOS), thereby tailoring the radiative and nonradiative decay rates.^{17,20–27} An optimal fluorescence enhancement factor requires a delicate balance of the excitation, radiative and nonradiative decay rates.^{12,13,28,29} To date, plasmonic structures have been developed to obtain fluorescence enhancement, also termed metal-enhanced fluorescence,³⁰ such as metallic layered structures,^{31,32} waveguides,³³ ordered structures,^{34,35} nanoantennas,^{36–39} nanoparticles^{12,13,40,41} to name just a few.

Compared to other plasmonic alternatives, core-shell nanoparticles possess unique advantages owing to their mass production capability with low cost chemical synthesis methods.^{42–49} With regard to tuning the localized surface plasmon resonance (LSPR) wavelength, metal shell particles are superior to dielectric shell particles. As it can be qualitatively understood already from the quasi-static analysis,⁵⁰ in the metal shell case one can tune the dipole LSPR between $\text{Re } \varepsilon_s = -3(\varepsilon_c + 2\varepsilon_h)/\{2[1 - (r_c/r_s)^3]\}$ for $r_s \rightarrow r_c$ and $\text{Re } \varepsilon_s = -2\varepsilon_h$ for $r_c \rightarrow 0$, where r_c and r_s are core and shell radii, and ε_c , ε_s and ε_h correspond to dielectric permittivities of a core, shell and host medium, respectively. For Ag and Au shells, this translates into the whole visible and near-infrared range simply by a control of the core-shell morphology, i.e. of the ratio r_c/r_s .^{42,43,50,51} In the dielectric shell case, the tunability limits are set between $\text{Re } \varepsilon_c = -2\varepsilon_h$ for $r_s \rightarrow r_c$ and $\text{Re } \varepsilon_c = -2\varepsilon_s$ for $r_c \rightarrow 0$,⁵⁰ and the resulting tunability is narrower and typically of the order of ~ 100 nm. For the same reason, initial search of fluorescence enhancement focused more on metal shell particles, whereas the use of metal-dielectric core-shell particles, apart of some preliminary work,^{45,46,52–60} has still remained to be underestimated in the current literature.

In what follows, we show that the neglect of dielectric shell particles has been largely undeserved. We searched for experimentally feasible metal-dielectric core-shell configurations with common Au and Ag cores and widely available dielectric shell materials (SiO_2 , Al_2O_3 , ZnO) whose refractive indices are higher than that of the host medium (air or water), for

optimal fluorescence enhancements. The outcome is that, in spite of relatively narrow tunability of the LSPR wavelength of those particles, there is still enough of design flexibility left for optimally designed nanoparticles to enable (i) comparable or even larger fluorescence enhancement as metal shells⁶¹ and (ii) significantly enhanced fluorescence compared to homogeneous metal particles,^{45,46,58–60} due to the efficient tailoring of the electric near-field and fluorescence decay rates by dielectric shell. Furthermore, the dielectric shell of a metal-dielectric core-shell nanoparticle (also called shell-isolated nanoparticle⁶⁰) provides a convenient way to separate the fluorescence emitter and the metallic component with a pre-determined distance, thus avoiding the quenching problem.^{12,45,52,57,62,63} In our simulations, we have employed a rigorous and computationally fast transfer matrix method, which can be viewed as an extension of the theory for homogeneous particles^{20–23} to a multilayered case with an arbitrary number of layers, to obtain the radiative and nonradiative decay rates,^{24,25} the electric field distribution,⁶⁴ and, as a result, the fluorescence enhancement factor.

2 Methods

Core-shell nanoparticle enhanced fluorescence can be described in two steps as shown in Figure 1, with the fluorescence emitter being modelled as an oscillating dipole.^{17,20–24} First, the core-shell nanoparticle locally enhances an electric field under a plane wave excitation, thereby amplifying the excitation rate of the fluorescence emitter in its proximity. Second, after being excited, the emitter itself radiates, and mutual interaction with the nanoparticle modifies the radiative and nonradiative decay rates of an emitter.^{13,18,22,39} Note that the fluorescence excitation and emission processes are treated independently (i.e. weak coupling) and the emitter is assumed to be below saturation.^{12,13}

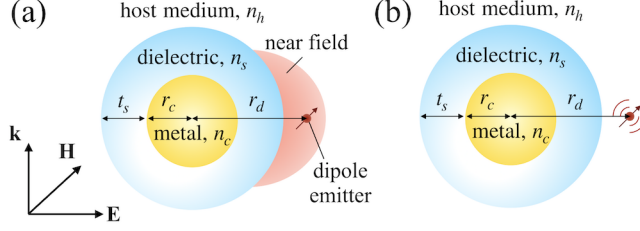


Figure 1: A conventional two-step model for nanoparticle enhanced fluorescence: (a) excitation process under plane wave illumination, and (b) emission process with dipole radiation. The origin of coordinates is located at the particle center.

2.1 Excitation process: electric field enhancement

Under a plane wave illumination, the electric field in j -th layer of a general multilayered core-shell nanoparticle, from the core ($j = 1$) up to the host medium ($j = N + 1$), where the number of layers in our case is $N = 2$, is expanded into multipole expansion:²⁴

$$\mathbf{E}_p(\mathbf{r}) = \sum_{p,L} [A_{pL}(j)\mathbf{J}_{pL}(k_j, \mathbf{r}) + B_{pL}(j)\mathbf{H}_{pL}(k_j, \mathbf{r})] . \quad (1)$$

Here $L = \ell, m$ is the composite angular momentum index with ℓ and m being the usual orbital and magnetic angular momentum numbers, the respective $p = E$ and $p = M$ denote electric (or TM) and magnetic (or TE) polarizations, $k_j = 2\pi n_j/\lambda$ is the wavenumber in j -th shell with refractive index n_j , λ is the incident wavelength, $A_{pL}(j)$ and $B_{pL}(j)$ are the expansion coefficients, $\mathbf{J}_{pL}(k_j, \mathbf{r})$ and $\mathbf{H}_{pL}(k_j, \mathbf{r})$ are vector multipoles.^{24,64} The expansion coefficients $A_{pL}(j)$ and $B_{pL}(j)$ can be obtained by matching the tangential components of the electromagnetic fields at each interface by implementing the recursive algorithm.

2.2 Emission process: radiative and nonradiative decay rates

The interaction between the dipole emission and the core-shell nanoparticle can be analytically solved using the transfer matrix method.^{24,65} A dipole emitter is assumed to be located at the radial distance r_d , which can be inside the shell or outside the core-shell nanoparticle.^{45–47,49,53–56,62} For non-magnetic core-shell particle and host, the radiative, γ_{rad} , and

nonradiative decay rates, γ_{nrad} , normalized with respect to the radiative decay rate in the free space (assumed to have the host permittivity), $\gamma_{\text{rad};0}$, can be obtained as:²⁴

$$\begin{aligned}
\frac{\gamma_{\text{rad}}^{\perp}}{\gamma_{\text{rad};0}} &= \frac{3}{2x_d^4} \frac{n_d}{n_h} \sum_{\ell} \ell(\ell+1)(2\ell+1) |f_{E\ell}(x_d)|^2, \\
\frac{\gamma_{\text{rad}}^{\parallel}}{\gamma_{\text{rad};0}} &= \frac{3}{4x_d^2} \frac{n_d}{n_h} \sum_{\ell} (2\ell+1) \left[|f_{M\ell}(x_d)|^2 + |f'_{E\ell}(x_d)|^2 \right], \\
\frac{\gamma_{\text{nrad}}^{\perp}}{\gamma_{\text{rad};0}} &= \frac{3k_d^3}{2x_d^4} \frac{1}{n_d n_h} \text{Im}(n_a^2) \sum_{\ell} \ell(\ell+1)(2\ell+1) I_{E\ell} |d_{E\ell}(x_d)|^2, \\
\frac{\gamma_{\text{nrad}}^{\parallel}}{\gamma_{\text{rad};0}} &= \frac{3k_d^3}{4x_d^2} \frac{1}{n_d n_h} \text{Im}(n_a^2) \sum_{\ell} (2\ell+1) \left[I_{M\ell} |d_{M\ell}(x_d)|^2 + I_{E\ell} |d'_{E\ell}(x_d)|^2 \right],
\end{aligned} \tag{2}$$

where the respective “ \perp ” and “ \parallel ” indicate the perpendicular (radial) and parallel (tangential) dipole orientation relative to the particle surface, n_a is the refractive index of the dissipative component with a non-zero imaginary part (i.e. the plasmonic metal core in our case), n_h is the refractive index of the host medium, $f_{p\ell}(x_d)$ and $d_{p\ell}(x_d)$ are linear combinations of Riccati-Bessel functions, $x_d = k_d r_d$, and $k_d = 2\pi n_d / \lambda$, where the subscript d corresponds to location of a dipole emitter. The symbols $I_{p\ell}$ represent volume integrals taken over any absorbing region, i.e. in our case over the entire metal core. Finally, the prime denotes the differentiation with respect to the argument in parentheses.

2.3 Fluorescence enhancement

For light intensities below dye saturation, the fluorescence enhancement factor can be expressed as the product of the excitation rate and the quantum yield, which is essentially related to the electric field distribution and dipole decay rates of the core-shell nanoparticle:

$$\frac{\eta_{\text{em}}}{\eta_{\text{em};0}} = \frac{\gamma_{\text{exc}}}{\gamma_{\text{exc};0}} \frac{q}{q_0}. \tag{3}$$

Here the subscript “0” indicates the respective quantity in the free space. The excitation rate can be expressed as $\gamma_{\text{exc}} \propto |\mathbf{E} \cdot \mathbf{d}|^2$, where \mathbf{E} is the local electric field at the emitters position which can be obtained from eq 1, and \mathbf{d} represents the dipole moment of the emitter. In our simulations we shall use both orientationally averaged electric field intensity and orientationally averaged decay rates. The orientationally averaged electric field intensity is to be understood as the field intensity averaged over a spherical surface of a given fixed radius r ,⁶⁴ whereas an orientationally averaged decay rate is determined at a fixed dipole position by averaging over all possible dipole orientations. The surface integrals of intensities can be performed analytically,⁶⁴ whereas orientation-averaged decay rates can be determined directly from eq 2 as $\gamma_{\text{nrad};\text{rad}} = (\gamma_{\text{nrad};\text{rad}}^{\perp} + 2\gamma_{\text{nrad};\text{rad}}^{\parallel})/3$. Fluorescence enhancement at a given radial position will be determined by substituting into eq 3 an average quantum yield

$$q = \frac{\gamma_{\text{rad}}/\gamma_{\text{rad};0}}{\gamma_{\text{rad}}/\gamma_{\text{rad};0} + \gamma_{\text{nrad}}/\gamma_{\text{rad};0} + (1 - q_0)/q_0}, \quad (4)$$

with the intrinsic quantum yield q_0 assumed, for simplicity, to be unity. The quantum yield accounts for the competition between the radiative and nonradiative decay rates. Note that $q \neq (q^{\perp} + 2q^{\parallel})/3$.

The above makes it clear that, although the core-shell far-field (i.e. scattering) properties can be, at least qualitatively, understood by the quasi-static analysis,^{50,66} the influence of near-fields on fluorescence is much more involved. Below, a systematic investigation is conducted taking into account these near-field effects to find optimal conditions for fluorescence enhancement.

3 Optimized core-shell configurations for fluorescence enhancement

The speed and robustness of our method allows us to perform an optimization study scanning over up to $\approx 10^5$ different core-shell configurations for each wavelength and for each shell material. The schematic of the structure is shown in Figure 1 displaying the core-shell nanoparticle with a metal core (with radius r_c and refractive index n_c) surrounded by a dielectric shell (with thickness t_s and refractive index n_s). The nanoparticle is embedded in a homogeneous medium with a refractive index n_h , which is set to be air ($n_h = 1$) or water ($n_h = 1.33$) in what follows. Au and Ag were selected as the core materials. For the sake of comparison with earlier results, Palik et al.⁶⁷ data of Au and Ag dielectric function were used in our simulations. Noteworthy, optimally synthesized Au and Ag cores may exhibit lower losses,⁶⁸ thereby facilitating even higher fluorescence enhancements.

Optimization results are obtained by scanning over different Au (Figure 2) and Ag (Figure 3) core radii within the interval $20 \leq r_c \leq 130$ nm and $5 \leq r_c \leq 70$ nm, correspondingly. We allow the shell thickness to vary within the interval $0 < t_s \leq 40$ nm and perform optimization for three different shell refractive indices 1.45, 1.76, 2.00, corresponding to typical values of SiO_2 , Al_2O_3 , ZnO , all that within 550–850 nm and 390–500 nm wavelength ranges for Au and Ag, respectively. The searched intervals for r_c and t_s are justified by the final results shown in Figures 2 and 3 and make use of the fact that too small metal cores cause an increased absorption resulting in relatively enhanced contribution of the nonradiative decay rate which reduces fluorescence. Dyes are assumed to have zero or a moderate Stokes shift of 25 nm, which are the typical values of Alexa fluorophores.

In general, larger fluorescence enhancement factor can be achieved with utilizing shells having higher refractive index. Interestingly, the maximum fluorescence enhancement of Au and Ag core-shell particles covers a large portion of the visible spectrum. For Au cores, the maximum fluorescence enhancement can be achieved between 620–700 nm irrespective of the

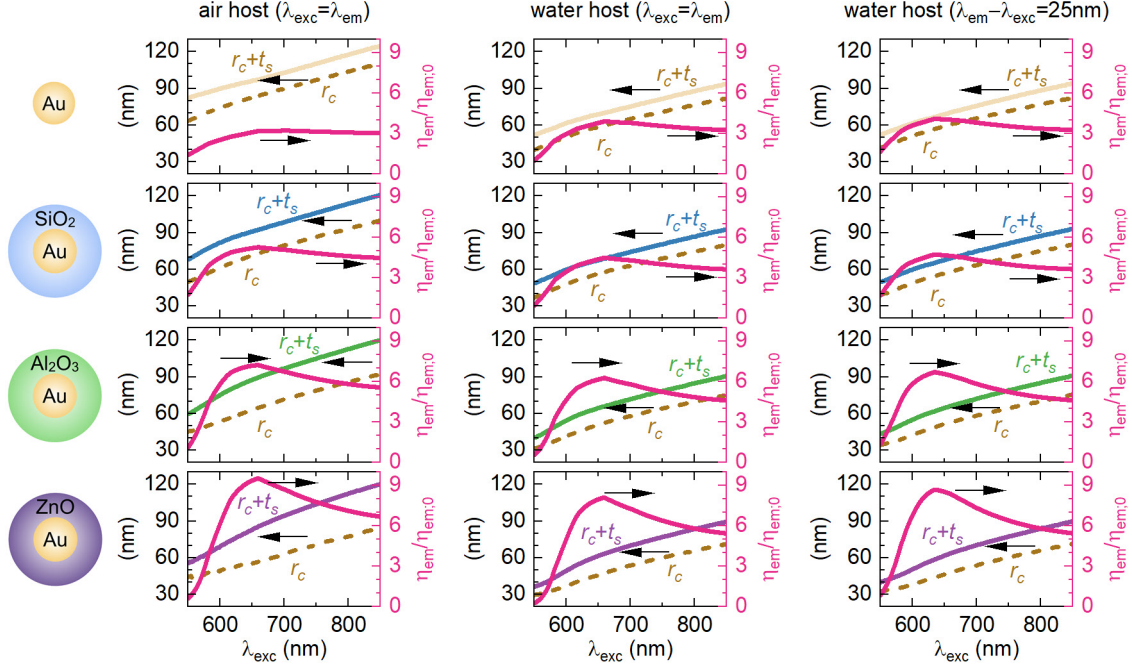


Figure 2: Optimal parameters (r_c, t_s) of Au@dielectric core-shell nanoparticles having maximum achievable fluorescence enhancement at a given excitation wavelength λ_{exc} for a dipole emitter located at 0.75 nm distance (given that a dye size is typically 1–2 nm) from a surface of a shell for nanoparticles with different materials of a shell, from top to bottom: bare Au nanoparticle, SiO₂ shell, Al₂O₃ shell, and ZnO shell. Nanoparticles are embedded in air or water host medium, and dyes are assumed to have zero or 25 nm Stokes shift ($\lambda_{\text{em}} - \lambda_{\text{exc}}$, where λ_{em} is the emission wavelength). For the bare Au nanoparticle, the actual distance between the dye and a metal surface is ($t_s + 0.75$) nm, which allows for a relevant comparison with core-shells. Both orientationally averaged electric field intensity⁶⁴ and average dipole orientation are used at each wavelength.

host (air or water), with the fluorescence enhancement overcoming that around homogeneous metal particle within the first near-infrared biological window (NIR-I) between 700–900 nm by a factor of ≈ 2 , when the shell refractive index $n_s \gtrsim 2$.

Silver has been known for long time as the best surface-enhanced Raman spectroscopy (SERS)⁶⁹ and plasmonic material.^{70,71} An evidence of this is seen also here in almost an order of magnitude higher maximum fluorescence enhancement (≈ 70) for Ag cores (Figure 3) than in the case of Au cores (≈ 9) (Figure 2), which is a consequence of weaker silver losses. This enables stronger enhancement of the near-field electric field intensities and the resulting excitation rate. Once a proper fluorescence enhancement peak builds up, the ratio of peak

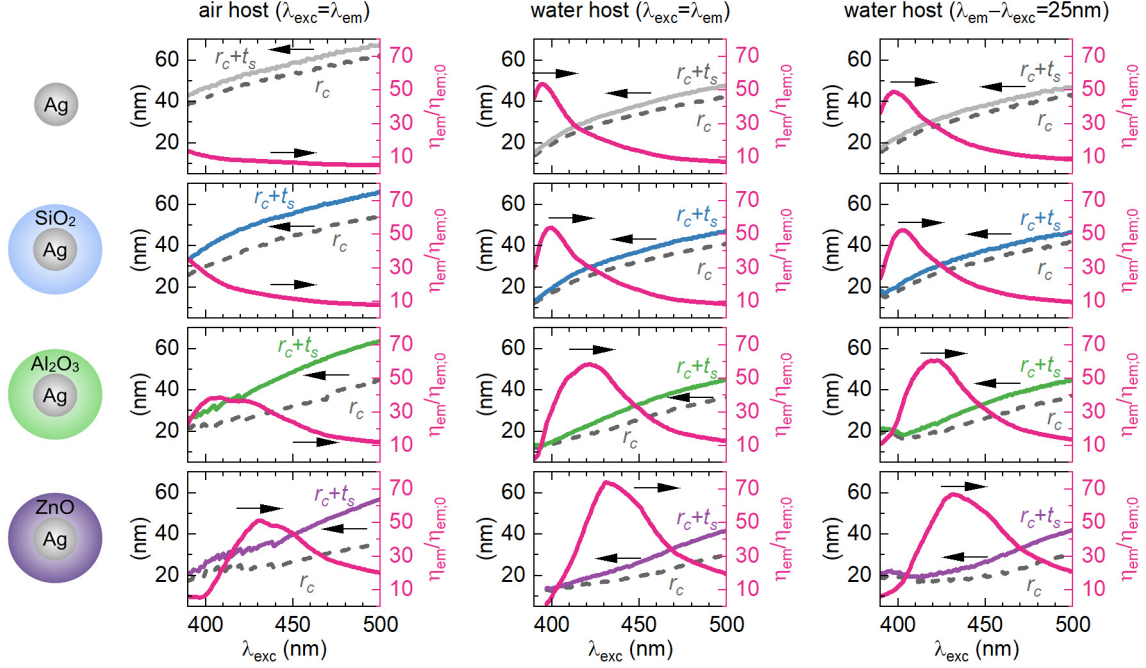


Figure 3: Same as in Figure 2, but for Ag as the core material. Due to strong absorption in Ag close to the LSPR of homogeneous Ag sphere, one observes pronounced fluorescence quenching, $\eta_{\text{em}}/\eta_{\text{em},0} \rightarrow 0$, for $\lambda_{\text{exc}} < 400$ nm in aqueous host. Almost an order of magnitude higher maximum fluorescence enhancement (≈ 70) can be achieved for Ag@dielectric core-shells than for Au@dielectric counterparts (≈ 9) of Figure 2.

fluorescence enhancement values with and without shell is not as high as that for Au cores. However, the difference in the peak values is significantly higher (≈ 20) than for Au cores (≈ 6). The effect of the Stokes shift on the maximum fluorescence enhancement is clearly visible in both core cases. Given that arbitrary Stokes shifts are, in principle, possible,⁷² the Stokes shifts could become another useful model parameter.

We conclude this section by an observation, which will be detailed below, that our average fluorescence results shown in Figures 2 and 3 can be easily exceeded by judiciously placing a low- q_0 fluorophore ($q_0 \approx 0.1$) at a hot-spot of the core-shell particle, with the fluorophore dipole moment properly oriented, which can generate a multiplication factor of $\gtrsim 25$ on top of the results shown in Figures 2, 3.

4 Discussion

An essential prerequisite for our simulations was recently reported efficient determination of orientationally averaged electric field intensities,^{64,73} which supplemented earlier efficient calculation of decay rates.²⁴ In essence, surface integrals of electric field intensity can be performed analytically⁶⁴ and the calculation of average intensity costs the same computational time as determining intensity at a given point. Below we discuss a number of different aspects related to our optimization results.

4.1 A critical role of the shell

The lesson to be learned from our simulations shown in Figures 2, 3 is obviously that the maximal fluorescence enhancement increases with the shell refractive index. This suggests even higher fluorescence enhancements by using shell materials such as Ta₂O₅ ($n_s \approx 2.16$), Nb₂O₅ ($n_s \approx 2.48$), TiO₂ ($n_s \gtrsim 2.55$), or Si ($n_s \gtrsim 3.7$). To get more insights about the position of, and the mechanism behind, the maximal fluorescence enhancement, we plot in Figure 4 in details near-field (NF) and far-field properties of Au@SiO₂ core-shell with optimal parameters to exhibit maximum achievable fluorescence at $\lambda = 642$ nm. An asymmetric Fano-like shape characterizing extinction, scattering and absorption spectra, local electric field enhancement, nonradiative and radiative decay rates, and fluorescence enhancement (Figures 4a-c,e,f) indicates an interference of different multipolar modes.^{74,75} As observed by Miroshnichenko,⁷⁵ the resonant NF enhancement (i.e. local field enhancement that controls the excitation rate, γ_{exc}) can be *red-shifted* in the Fano case by as much as ≈ 50 nm relative to the resonant scattering (i.e. LSPR) for metal-dielectric core-shell particles. The NF red-shift has been known for a long time⁷⁶ and its origin can be accounted for by a simple harmonic oscillator model of plasmon oscillations.⁷⁷ The maximum of radiative decay rate shown in Figure 4e coincides with the maximum of NF at the outer shell surface (Figure 4b), which is seen as the main origin of the *red-shift* of the maximum of fluorescence enhancement

(Figure 4f) relative to the LSPR (Figure 4a). An additional small red-shift of the maximum of fluorescence enhancement (Figure 4f) relative to the maximum of radiative decay rate γ_{rad} (Figure 4e) is due to increasing quantum yield (Figure 4d). Note in passing that it has been noted for homogeneous Ag particles that the highest fluorescence enhancement is obtained for an emission wavelength red-shifted from the LSPR,¹³ yet no explanation has been given.

Of the same magnitude as the red-shift is the *blue shift* of the maximum of nonradiative decay rate (Figure 4c) relative to the LSPR (Figure 4a). The LSPR position coincides with the maximum of field intensity at the Au core surface (Figure 4b) and the maximum of Q_{ext} (Figure 4a). The position of the maximum nonradiative decay rate γ_{nrad} , which essentially coincides with Q_{abs} , is blue-shifted to the LSPR. The difference in the shape of the peaks of γ_{nrad} and Q_{abs} is attributed to a fact that the former describes power loss of a dipole emitter at the shell surface, whereas the latter is the measure of absorption of incident plane arriving from the spatial infinity. The above red and blue shifts relative to the LSPR of corresponding optimized core-shell particle provide important design rules for selected application. Note in passing that there is a number of applications where not only fluorescence *enhancement* but also an efficient fluorescence *quenching* is highly desirable.⁷⁸

In a Drude-like region above bulk plasma wavelength ($\lambda_p \approx 328$ nm for Ag and $\lambda_p \approx 226$ nm for Au), the loss tangent (i.e. the ratio $|\text{Im } \epsilon / \text{Re } \epsilon|$) of a noble metal dielectric function decreases with increasing wavelength. Therefore, the use of shells with larger refractive indices, which increases the red shift of their LSPR, and consequently of their NF maximum, creates increasingly favourable conditions for fluorescence enhancement by reducing (increasing) the overall contribution of nonradiative (radiative) decay rates. At the same time, the boundary condition at the shell-host interface for the radial components of electric field, $\epsilon_s \mathbf{E}_s^\perp = \epsilon_h \mathbf{E}_h^\perp$, implies that \mathbf{E}^\perp experiences a jump by the factor of ϵ_s / ϵ_h at the host, with \mathbf{E}^\parallel being continuous across the shell-host interface. Obviously, the jump in field intensity values at the shell surface becomes more pronounced with larger n_s , enabling to achieve quite large electric field enhancement at the shell-host interface even for relatively

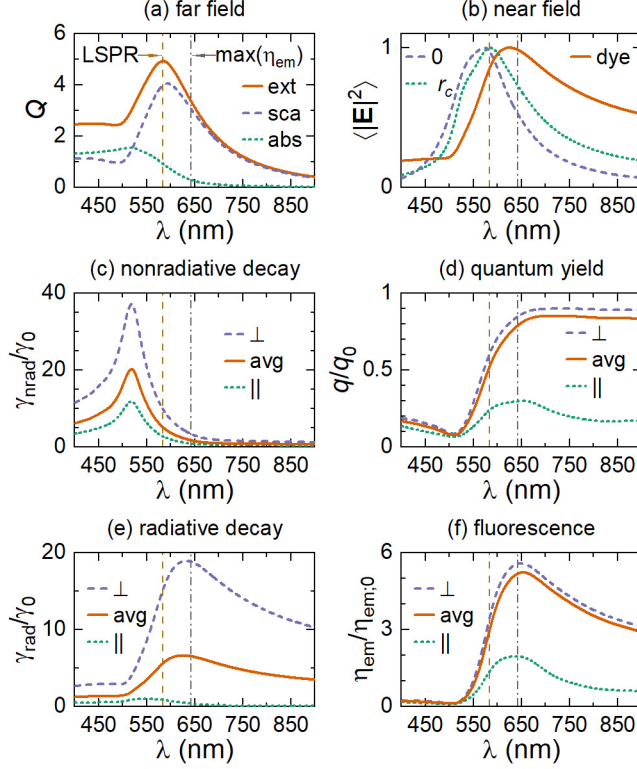


Figure 4: An explanation of the red shift of the maximum fluorescence of Au@SiO₂ core-shell particle with $r_c = 70$ nm and $t_s = 19.7$ nm tuned to exhibit optimal fluorescence enhancement at $\lambda = 642$ nm (vertical dash-dot line) in air host relative to its LSPR at $\lambda = 583$ nm (vertical dashed line): (a) extinction, scattering and absorption efficiencies; (b) orientationally averaged electric field intensity at the center of the Au core (0), at the metal side surface of Au core at r_c , and at the dye location at 0.75 nm distance from the shell surface (dye), each curve is normalized to show the red-shift of the peak moving from the core center to the dye location; (c),(e) nonradiative and radiative decay rates for radial (\perp) and tangential (\parallel) orientation of the dipole emitter, and orientationally averaged (avg); (d) quantum yield, eq 4, calculated for the respective orientations of the dipole emitter (radial, tangential, and orientationally averaged); (f) fluorescence enhancement, eq 3. Except for quantum yield, all other curves exhibit an asymmetric Fano-like shape.

thick shells (Figure 5b; Figures S3, S4, see Supporting Information).

Note that the procedure used in Figures 2 and 3 for the search of optimal $(r_{c;\text{opt}}, t_{s;\text{opt}})$ configurations implies the fluorescence enhancement to be the largest possible at a given wavelength $\lambda_{\text{exc;opt}}$. This, however, does not restrict the same core-shell to exhibit even larger fluorescence enhancement at another wavelength $\lambda_{\text{exc}} \neq \lambda_{\text{exc;opt}}$, which is clearly observed in Figure 5e. Nonetheless, the maxima in Figure 5f, which perfectly correspond to $t_{s;\text{opt}}$, confirm that $(r_{c;\text{opt}}, t_{s;\text{opt}})$ configurations indeed provide optimal $\eta_{\text{em}}/\eta_{\text{em},0}$ at $\lambda_{\text{exc;opt}}$ (cf. Figure S2,

see Supporting Information).

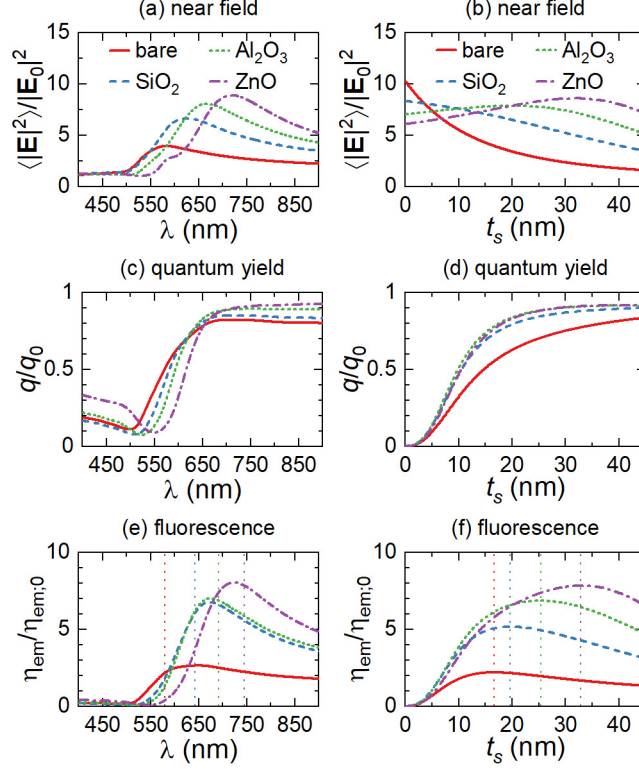


Figure 5: The impact of shells from different dielectrics on the fluorescence enhancement of $r_c = 70$ nm Au nanoparticle in air host. Wavelength- (left) and shell-thickness- (right) dependent: (a),(b) orientationally averaged electric field intensity at the dye location at 0.75 nm distance from the shell surface; (c),(d) quantum yield, eq 4; (e),(f) fluorescence enhancement, eq 3. Vertical dotted lines in (e),(f) show the respective wavelengths and corresponding optimal shell thicknesses to reach maximum fluorescence enhancement for bare Au core ($\lambda = 580$ nm and $t_s = 16.7$ nm), Au@SiO₂ ($\lambda = 642$ nm and $t_s = 19.7$ nm), Au@Al₂O₃ ($\lambda = 691$ nm and $t_s = 25.4$ nm), Au@ZnO ($\lambda = 745$ nm and $t_s = 32.8$ nm). Wavelength-dependent plots (left) are presented for optimal shell thicknesses denoted by vertical lines in (f), while shell-thickness-dependent plots (right) show corresponding quantities at wavelengths denoted by vertical lines in (e).

4.2 Comparison with an experiment

Our optimization results of Sec. 3 provide general guidelines for achieving the highest possible fluorescence enhancements. Before comparing them against an experiment, the following has to be taken into account. First, our simulations assuming either zero Stokes shift, or a model Stokes shift of 25 nm have to be adjusted to the Stokes shift of the fluorophore used.

The Stokes shift is strongly dependent on a fluorophore used and can be much larger than the 25 nm.⁷² Second, optimally fabricated Au and Ag cores may exhibit lower losses⁶⁸ than those following from the data of Palik et al⁶⁷ used in our simulations, thereby facilitating even higher fluorescence enhancements. Third, optimization results of Sec. 3 assumed orientationally averaged electric field intensity and average dipole orientation. On judiciously placing fluorophore at hot spots of electric field intensity with the fluorophore dipole moment properly oriented such a local fluorescence enhancement can be up to ≈ 2.5 times stronger (Figure S9, see Supporting Information). Last but not the least, simulations of Sec. 3 presumed intrinsic quantum yield $q_0 = 1$. In this regard, any $q_0 < 1$ will increase the denominator of eq 4 by $(1 - q_0)/q_0$. However, for moderate $0.1 \leq q_0 < 1$ and for the metal-dye separations studied, this contribution is typically negligible compared to other two terms in the denominator (e.g. $\gamma_{\text{nrad}}/\gamma_{\text{rad};0}$). Hence $0.1 \leq q_0 < 1$ will hardly change the resulting quantum yield q of eq 4. However, such a moderate $0.1 \leq q_0 < 1$ will, according to eq 3, significantly increase the resulting fluorescence enhancement shown in Figures 2, 3 by a factor of $1/q_0$. For instance, in the case of low $q_0 = 0.36$ carboxyfluorescein (FAM) and Au@SiO₂ core-shell nanoparticles with $r_c = 29.5$ nm of Ref. 45 [Table 1; Figure 2B] this amounts to the factor of $1/q_0 \approx 2.8$. On the other hand, for cascade yellow (CYe) having an intrinsic quantum efficiency of about $q_0 = 0.56$ and Ag@SiO₂ core-shell nanoparticles of Ref. 45 [Table 1; Figure 3] this amounts to the factor of $1/q_0 \approx 1.78$. Therefore, when comparing with experiment, a low- q_0 dye ($q_0 \approx 0.1$) placed at a hot-spot of the core-shell particle can easily generate a multiplication factor of ≈ 25 by which the results shown in Figures 2, 3 are to be multiplied. Not surprisingly, initial experiments observed significant fluorescence enhancements especially with low- q_0 dyes.^{45,46}

4.3 Comparison with metal shells

The highest reported fluorescence enhancements for dielectric ($n = 3.5$) core and Ag shell of comparable sizes tuned to the Fano resonance⁶¹ were in the case of radially oriented

dipole located at the hot spot reaching nearly the value of 50, whereas the enhancements for tangentially oriented dipole hardly exceeded the value of 2.5. This results in the dipole orientation averaged fluorescence enhancement of ≈ 18 . Our results for dielectric shells presented in Figure 3 show almost *four-times* larger averaged fluorescence enhancement with much lower shell refractive index ($n = 2$) and without the need of keeping the dipole emitter at a hot spot. Here one notable difference between the homogeneous sphere and metal-dielectric core-shell on one hand, and a dielectric-metal core-shell on the other hand, is that in the former case the areas of highest field enhancement are located near the particle poles on the rotation axis *parallel* to the incident polarization direction, whereas in metallic shells the areas of highest field enhancement are located near the particle poles on the rotation axis *perpendicular* to the incident polarization.⁷⁹

4.4 Quasi-static approximation

The Gersten and Nitzan (GN) quasi-static approximation for determining decay rates,⁸⁰ which makes use of particle multipolar polarizabilities, α_ℓ , has been known to provide a very good approximation of radiative and nonradiative decay rates in the case of small homogeneous particles.⁸¹ A dipolar polarizability with the account of dynamic depolarization and radiative correction⁸² (see Sec. 3 in Supporting Information for details) enables rather precise description of the scattering properties of core-shell particles. Nevertheless, the GN approximation⁸⁰ largely fails to describe the nonradiative decays rates for the core-shell configurations studied here, as shown in Figure 6d. Although the modified long wavelength approximation (MLWA) and its variants^{66,82} capture well the far-field properties (e.g. scattering), they do not perform so well in capturing the near-field properties (e.g. fluorescence). An indirect indication of this is that the radiative decay rates, requiring only dipole polarizability in the GN approximation, were approximated much better than the nonradiative decay rates, which require all multipole polarizabilities.

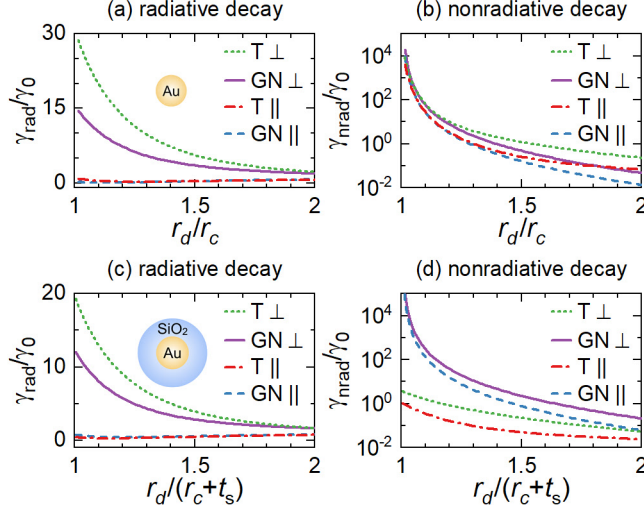


Figure 6: Radiative (left) and nonradiative (right) decay rates at a distance r from a center of nanoparticle, calculated via transfer-matrix method (T) and the Gersten and Nitzan (GN) quasi-static approximation for bare Au nanoparticle (top) and for Au@SiO₂ core-shell for radial (\perp) and tangential (\parallel) orientation of the dipole emitter. The parameters are given in Figure 5 caption.

5 Conclusion

Large scale simulations were performed by means of the transfer-matrix method to reveal optimal conditions for metal-dielectric core-shell particles to induce an optimal fluorescence of a fluorophore on their surface. In the simulations, limited to Au and Ag cores and common dielectric shell materials (SiO₂, Al₂O₃, ZnO), we have (i) determined the optimal size of metal core and shell thickness for reaching a maximum fluorescence enhancement for each emission wavelength, and then (ii) determined overall maximum fluorescence enhancements taken over entire wavelength interval. The peak value of maximum achievable fluorescence enhancement factors of core-shell nanoparticles can reach up to 9 or 70 for Au and Ag cores within 600 – 700 nm and 400 – 450 nm wavelength ranges, respectively, which is much larger than that for corresponding homogeneous metal nanoparticles. Replacing air by an aqueous host has a dramatic effect of nearly halving the sizes of optimal core-shell configurations at the maximum of achievable fluorescence. In the case of Au cores, the fluorescence enhancements for wavelengths within the first near-infrared biological window (NIR-I) between 700 and

900 nm can be improved twofold compared to homogeneous Au particle when the shell refractive index $n_s \gtrsim 2$. Given that the maximum achievable fluorescence enhancement factor increases with the shell refractive index, even higher fluorescence enhancements could be possible by using shell materials such as Ta_2O_5 ($n_s \approx 2.16$), Nb_2O_5 ($n_s \approx 2.48$), TiO_2 ($n_s \gtrsim 2.55$), or Si ($n_s \gtrsim 3.7$). As a rule of thumb, the wavelength region of optimal fluorescence (maximal nonradiative decay) turned out to be red-shifted (blue-shifted) by as much as 50 nm relative to the LSPR of corresponding optimized core-shell particle. The main contribution to the red-shift was determined to be provided by the red shift of the near-field enhancement relative to the LSPR. Our results provide important design rules and general guidelines for enabling versatile platforms for selected applications such as imaging, light source, and biological applications. Our results for near-field enhancement also have direct relevance to designing optimal SERS platforms.

Acknowledgement

CAEP Innovation Grant, PRC China (Grant No.CX20200011), Science Challenge Project, PRC China (Grant No.TZ2016003).

Supporting Information Available

The following files are available free of charge. Benchmarking with the finite-element method; additional data for extinction spectra, electric field enhancement, radiative and non-radiative decay rates, quantum yields and fluorescence enhancement for core-shell nanoparticles; quasi-static equations.

References

- (1) Stehr, F.; Stein, J.; Schueder, F.; Schwille, P.; Jungmann, R. Flat-top TIRF illumination boosts DNA-PAINT imaging and quantification. *Nature Communications* **2019**, *10*, 1268.
- (2) Ray, S.; Widom, J. R.; Walter, N. G. Life under the microscope: Single-molecule fluorescence highlights the RNA world. *Chemical Reviews* **2018**, *118*, 4120–4155.
- (3) Bower, A. J.; Li, J.; Chaney, E. J.; Marjanovic, M.; Spillman, D. R.; Boppart, S. A. High-speed imaging of transient metabolic dynamics using two-photon fluorescence lifetime imaging microscopy. *Optica* **2018**, *5*, 1290–1296.
- (4) Garcia, M.; Edmiston, C.; York, T.; Marinov, R.; Mondal, S.; Zhu, N.; Sudlow, G. P.; Akers, W. J.; Margenthaler, J.; Achilefu, S.; Liang, R.; Zayed, M. A.; Pepino, M. Y.; Gruev, V. Bio-inspired imager improves sensitivity in near-infrared fluorescence image-guided surgery. *Optica* **2018**, *5*, 413–422.
- (5) Park, S.-J.; Kim, B.; Choi, S.; Balasubramaniam, S.; Lee, S.-C.; Lee, J. Y.; Kim, H. S.; Kim, J.-Y.; Kim, J.-J.; Lee, Y.-A.; Kang, N.-Y.; Kim, J.-S.; Chang, Y.-T. Imaging inflammation using an activated macrophage probe with Slc18b1 as the activation-selective gating target. *Nature Communications* **2019**, *10*, 1111.
- (6) Andersen, C. M.; Mortensen, G. Fluorescence spectroscopy: a rapid tool for analyzing dairy products. *Journal of Agricultural and Food Chemistry* **2008**, *56*, 720–729.
- (7) Lu, C.; Zhang, P.; Chen, S.; Zhu, J.; Xu, X.; Huang, H. Fluorescence spectrum photobleaching analysis for distinguishing microorganisms (bacteria and fungi) from other particles in air. *Optics Express* **2018**, *26*, 28902–28917.
- (8) Schmidt, T. D.; Lampe, T.; Sylvinson M. R., D.; Djurovich, P. I.; Thompson, M. E.;

- Brütting, W. Emitter orientation as a key parameter in organic light-emitting diodes. *Physical Review Applied* **2017**, *8*, 037001.
- (9) Yang, Y.; Zheng, Y.; Cao, W.; Titov, A.; Hyvonen, J.; Manders, J. R.; Xue, J.; Holloway, P. H.; Qian, L. High-efficiency light-emitting devices based on quantum dots with tailored nanostructures. *Nature Photonics* **2015**, *9*, 259–266.
- (10) Reimer, M. E.; Cher, C. The quest for a perfect single-photon source. *Nature Photonics* **2019**, *13*, 734–736.
- (11) Xu, L.; Yuan, H.; Zhang, N.; Zhang, J.; Bian, G.; Fan, P.; Li, M.; Zhang, C.; Zhai, Y.; Fang, J. High-efficiency fluorescence collection for NV- center ensembles in diamond. *Optics Express* **2019**, *27*, 10787–10797.
- (12) Anger, P.; Bharadwaj, P.; Novotny, L. Enhancement and quenching of single-molecule fluorescence. *Physical Review Letters* **2006**, *96*, 113002.
- (13) Bharadwaj, P.; Novotny, L. Spectral dependence of single molecule fluorescence enhancement. *Optics Express* **2007**, *15*, 14266–14274.
- (14) Bharadwaj, P.; Deutsch, B.; Novotny, L. Optical antennas. *Advances in Optics and Photonics* **2009**, *1*, 438–483.
- (15) Fothergill, S. M.; Joyce, C.; Xie, F. Metal enhanced fluorescence biosensing: from ultra-violet towards second near-infrared window. *Nanoscale* **2018**, *10*, 20914–20929.
- (16) Li, J.-F.; Li, C.-Y.; Aroca, R. F. Plasmon-enhanced fluorescence spectroscopy. *Chemical Society Reviews* **2017**, *46*, 3962–3979.
- (17) Ford, G.; Weber, W. Electromagnetic interactions of molecules with metal surfaces. *Physics Reports* **1984**, *113*, 195–287.
- (18) Sun, S.; Wu, L.; Bai, P.; Png, C. E. Fluorescence enhancement in visible light: dielectric or noble metal? *Physical Chemistry Chemical Physics* **2016**, *18*, 19324–19335.

- (19) Dong, J.; Zhang, Z.; Zheng, H.; Sun, M. Recent progress on plasmon-enhanced fluorescence. *Nanophotonics* **2015**, *4*, 472–490.
- (20) Ruppin, R. Decay of an excited molecule near a small metal sphere. *Journal of Chemical Physics* **1982**, *76*, 1681–1684.
- (21) Chew, H. Transition rates of atoms near spherical surfaces. *Journal of Chemical Physics* **1987**, *87*, 1355–1360.
- (22) Chew, H. Radiation and lifetimes of atoms inside dielectric particles. *Physical Review A* **1988**, *38*, 3410–3416.
- (23) Kim, Y. S.; Leung, P.; George, T. F. Classical decay rates for molecules in the presence of a spherical surface: A complete treatment. *Surface Science* **1988**, *195*, 1–14.
- (24) Moroz, A. A recursive transfer-matrix solution for a dipole radiating inside and outside a stratified sphere. *Ann. Phys. (NY)* **2005**, *315*, 352–418.
- (25) Moroz, A. Spectroscopic properties of a two-level atom interacting with a complex spherical nanoshell. *Chemical Physics* **2005**, *317*, 1–15.
- (26) Girard, C.; Dujardin, E.; Marty, R.; Arbouet, A.; des Francs, G. C. Manipulating and squeezing the photon local density of states with plasmonic nanoparticle networks. *Physical Review B* **2010**, *81*, 153412.
- (27) Guo, K.; Verschuuren, M. A.; Koenderink, A. F. Superresolution imaging of the local density of states in plasmon lattices. *Optica* **2016**, *3*, 289–298.
- (28) Sun, S.; Li, M.; Du, Q.; Png, C. E.; Bai, P. Metal-dielectric hybrid dimer nanoantenna: coupling between surface plasmons and dielectric resonances for fluorescence enhancement. *Journal of Physical Chemistry C* **2017**, *121*, 12871–12884.

- (29) Ringler, M.; Schwemer, A.; Wunderlich, M.; Nichtl, A.; Kürzinger, K.; Klar, T. A.; Feldmann, J. Shaping emission spectra of fluorescent molecules with single plasmonic nanoresonators. *Physical Review Letters* **2008**, *100*, 203002.
- (30) Geddes, C.; Lakowicz, J. Metal-enhanced fluorescence. *Journal of Fluorescence* **2002**, *12*, 121–129.
- (31) Akimov, Y.; Sun, S. Spacer-controlled emission of randomly oriented fluorophores enhanced with surface plasmon-polaritons. *Physical Chemistry Chemical Physics* **2017**, *19*, 8706–8714.
- (32) Huang, C.-J.; Dostalek, J.; Sessitsch, A.; Knoll, W. Long-range surface plasmon-enhanced fluorescence spectroscopy biosensor for ultrasensitive detection of *E. coli* O157:H7. *Analytical Chemistry* **2011**, *83*, 674–677.
- (33) Wu, M.; Liu, W.; Hu, J.; Zhong, Z.; Rujiralai, T.; Zhou, L.; Cai, X.; Ma, J. Fluorescence enhancement in an over-etched gold zero-mode waveguide. *Optics Express* **2019**, *27*, 19002–19018.
- (34) Brolo, A. G.; Kwok, S. C.; Moffitt, M. G.; Gordon, R.; Riordon, J.; Kavanagh, K. L. Enhanced fluorescence from arrays of nanoholes in a gold film. *Journal of the American Chemical Society* **2005**, *127*, 14936–14941.
- (35) Guo, S.-H.; Heetderks, J. J.; Kan, H.-C.; Phaneuf, R. J. Enhanced fluorescence and near-field intensity for Ag nanowire/nanocolumn arrays: evidence for the role of surface plasmon standing waves. *Optics Express* **2008**, *16*, 18417–18425.
- (36) Ma, L.; Sun, S.; Zhang, T.; Li, R.; Du, Q.; Zhang, J.; Li, M. Highly-symmetrical plasmonic nanoantenna for fluorescence enhancement and polarization preservation of arbitrarily oriented fluorophore. *Optical Materials Express* **2018**, *8*, 3770–3786.

- (37) Kinkhabwala, A.; Yu, Z.; Fan, S.; Avlasevich, Y.; Müllen, K.; Moerner, W. E. Large single-molecule fluorescence enhancements produced by a bowtie nanoantenna. *Nature Photonics* **2009**, *3*, 654–657.
- (38) Sun, S.; Li, R.; Li, M.; Du, Q.; Png, C. E.; Bai, P. Hybrid mushroom nanoantenna for fluorescence enhancement by matching the Stokes shift of the emitter. *Journal of Physical Chemistry C* **2018**, *122*, 14771–14780.
- (39) Sun, S.; Zhang, T.; Liu, Q.; Ma, L.; Du, Q.; Duan, H. Enhanced directional fluorescence emission of randomly oriented emitters via a metal-dielectric hybrid nanoantenna. *Journal of Physical Chemistry C* **2019**, *123*, 21150–21160.
- (40) Tam, F.; Goodrich, G. P.; Johnson, B. R.; Halas, N. J. Plasmonic enhancement of molecular fluorescence. *Nano Letters* **2007**, *7*, 496–501.
- (41) Fan, Z.; Sun, L.; Huang, Y.; Wang, Y.; Zhang, M. Bioinspired fluorescent dipeptide nanoparticles for targeted cancer cell imaging and real-time monitoring of drug release. *Nature Nanotechnology* **2016**, *11*, 388–394.
- (42) Oldenburg, S.; Averitt, R.; Westcott, S.; Halas, N. Nanoengineering of optical resonances. *Chemical Physics Letters* **1998**, *288*, 243–247.
- (43) Graf, C.; van Blaaderen, A. Metallodielectric colloidal core-shell particles for photonic applications. *Langmuir* **2002**, *18*, 524–534.
- (44) Graf, C.; Vossen, D. L. J.; Imhof, A.; van Blaaderen, A. A general method to coat colloidal particles with silica. *Langmuir* **2003**, *19*, 6693–6700.
- (45) Tovmachenko, O. G.; Graf, C.; van den Heuvel, D. J.; van Blaaderen, A.; Gerritsen, H. C. Fluorescence enhancement by metal-core/silica-shell nanoparticles. *Advanced Materials* **2006**, *18*, 91–95.

- (46) Aslan, K.; Wu, M.; Lakowicz, J. R.; Geddes, C. D. Fluorescent core-shell Ag@SiO₂ nanocomposites for metal-enhanced fluorescence and single nanoparticle sensing platforms. *Journal of the American Chemical Society* **2007**, *129*, 1524–1525.
- (47) Guerrero, A. R.; Aroca, R. F. Surface-enhanced fluorescence with shell-isolated nanoparticles (SHINEF). *Angewandte Chemie International Edition* **2011**, *50*, 665–668.
- (48) Montaña-Priede, J. L.; Coelho, J. P.; Guerrero-Martínez, A.; Peña-Rodríguez, O.; Pal, U. Fabrication of monodispersed Au@SiO₂ nanoparticles with highly stable silica layers by ultrasound-assisted Stöber method. *Journal of Physical Chemistry C* **2017**, *121*, 9543–9551.
- (49) Xu, J.; Zhang, Y.-J.; Yin, H.; Zhong, H.-L.; Su, M.; Tian, Z.-Q.; Li, J.-F. Shell-isolated nanoparticle-enhanced Raman and fluorescence spectroscopies: Synthesis and applications. *Advanced Optical Materials* **2018**, *6*, 1701069.
- (50) Neeves, A. E.; Birnboim, M. H. Composite structures for the enhancement of nonlinear-optical susceptibility. *Journal of the Optical Society of America B* **1989**, *6*, 787–796.
- (51) Averitt, R. D.; Sarkar, D.; Halas, N. J. Plasmon resonance shifts of Au-coated Au₂S nanoshells: Insight into multicomponent nanoparticle growth. *Physical Review Letters* **1997**, *78*, 4217–4220.
- (52) Reineck, P.; Gómez, D.; Ng, S. H.; Karg, M.; Bell, T.; Mulvaney, P.; Bach, U. Distance and wavelength dependent quenching of molecular fluorescence by Au@SiO₂ core-shell nanoparticles. *ACS Nano* **2013**, *7*, 6636–6648.
- (53) Lu, L.; Qian, Y.; Wang, L.; Ma, K.; Zhang, Y. Metal-enhanced fluorescence-based core-shell Ag@SiO₂ nanoflares for affinity biosensing via target-induced structure switching of aptamer. *ACS Applied Materials & Interfaces* **2014**, *6*, 1944–1950.

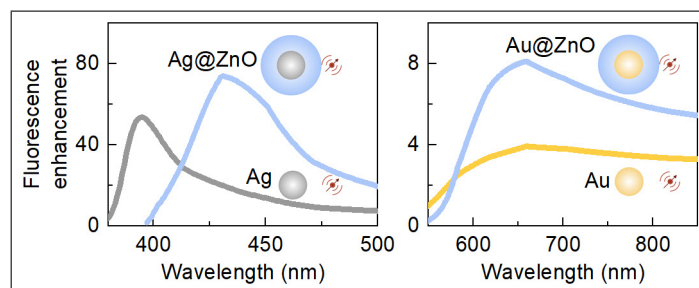
- (54) Wang, H.-S.; Wang, C.; He, Y.-K.; Xiao, F.-N.; Bao, W.-J.; Xia, X.-H.; Zhou, G.-J. Core-shell Ag@SiO₂ nanoparticles concentrated on a micro/nanofluidic device for surface plasmon resonance-enhanced fluorescent detection of highly reactive oxygen species. *Analytical Chemistry* **2014**, *86*, 3013–3019.
- (55) Pang, Y.; Rong, Z.; Wang, J.; Xiao, R.; Wang, S. A fluorescent aptasensor for H5N1 influenza virus detection based-on the core-shell nanoparticles metal-enhanced fluorescence (MEF). *Biosensors and Bioelectronics* **2015**, *66*, 527–532.
- (56) Planas, O.; Macia, N.; Agut, M.; Nonell, S.; Heyne, B. Distance-dependent plasmon-enhanced singlet oxygen production and emission for bacterial inactivation. *Journal of the American Chemical Society* **2016**, *138*, 2762–2768.
- (57) Walters, C. M.; Pao, C.; Gagnon, B. P.; Zamecnik, C. R.; Walker, G. C. Bright surface-enhanced Raman scattering with fluorescence quenching from silica encapsulated J-aggregate coated gold nanoparticles. *Advanced Materials* **2018**, *30*, 1705381.
- (58) Niu, J.-X.; Pan, C.-D.; Liu, Y.-T.; Lou, S.-T.; Wu, E.; Wu, B.-T.; Zhang, X.-L.; Jin, Q.-Y. Plasmon-enhanced fluorescence of submonolayer porphyrins by silver-polymer core-shell nanoparticles. *Optics Express* **2018**, *26*, 3489–3496.
- (59) Camacho, S. A.; Aoki, P. H. B.; Albella, P.; Oliveira, O. N.; Constantino, C. J. L.; Aroca, R. F. Increasing the enhancement factor in plasmon-enhanced fluorescence with shell-isolated nanoparticles. *Journal of Physical Chemistry C* **2016**, *120*, 20530–20535.
- (60) Meng, M.; Zhang, F.-L.; Yi, J.; Lin, L.-H.; Zhang, C.-L.; Bodappa, N.; Li, C.-Y.; Zhang, S.-J.; Aroca, R. F.; Tian, Z.-Q.; Li, J.-F. Shell-isolated nanoparticle-enhanced phosphorescence. *Analytical Chemistry* **2018**, *90*, 10837–10842.
- (61) Arruda, T. J.; Bachelard, R.; Weiner, J.; Slama, S.; Courteille, P. W. Fano resonances and fluorescence enhancement of a dipole emitter near a plasmonic nanoshell. *Physical Review A* **2017**, *96*, 043869.

- (62) Noginov, M. A.; Zhu, G.; Belgrave, A. M.; Bakker, R.; Shalae, V. M.; Nari-
manov, E. E.; Stout, S.; Herz, E.; Suteewong, T.; Wiesner, U. Demonstration of a
spaser-based nanolaser. *Nature* **2009**, *460*, 1110–1112.
- (63) Acuna, G. P.; Bucher, M.; Stein, I. H.; Steinhauer, C.; Kuzyk, A.; Holzmeister, P.;
Schreiber, R.; Moroz, A.; Stefani, F. D.; Liedl, T.; Simmel, F. C.; Tinnefeld, P. Dis-
tance dependence of single-fluorophore quenching by gold nanoparticles studied on DNA
origami. *ACS Nano* **2012**, *6*, 3189–3195.
- (64) Rasskazov, I. L.; Moroz, A.; Carney, P. S. Electromagnetic energy in multilayered
spherical particles. *Journal of the Optical Society of America A* **2019**, *36*, 1591–1601.
- (65) Rasskazov, I. L.; Wang, L.; Murphy, C. J.; Bhargava, R.; Carney, P. S. Plasmon-
enhanced upconversion: engineering enhancement and quenching at nano and macro
scales. *Optical Materials Express* **2018**, *8*, 3787–3804.
- (66) Chung, H. Y.; Leung, P. T.; Tsai, D. P. Dynamic modifications of polarizability for
large metallic spheroidal nanoshells. *Journal of Chemical Physics* **2009**, *131*, 124122.
- (67) Palik, E. D. *Handbook of optical constants of solids II*; Academic Press: New York,
1998; p 1096.
- (68) McPeak, K. M.; Jayanti, S. V.; Kress, S. J. P.; Meyer, S.; Iotti, S.; Rossinelli, A.;
Norris, D. J. Plasmonic films can easily be better: Rules and recipes. *ACS Photonics*
2015, *2*, 326–333.
- (69) Moskovits, M. Surface-enhanced spectroscopy. *Reviews of Modern Physics* **1985**, *57*,
783–826.
- (70) Moroz, A. Three-dimensional complete photonic-band-gap structures in the visible.
Physical Review Letters **1999**, *83*, 5274–5277.

- (71) Moroz, A. Photonic crystals of coated metallic spheres. *Europhysics Letters (EPL)* **2000**, *50*, 466–472.
- (72) Ren, T.-B.; Xu, W.; Zhang, W.; Zhang, X.-X.; Wang, Z.-Y.; Xiang, Z.; Yuan, L.; Zhang, X.-B. A general method to increase Stokes shift by introducing alternating vibronic structures. *Journal of the American Chemical Society* **2018**, *140*, 7716–7722.
- (73) Rasskazov, I. L. <https://gitlab.com/iliarasskazov/stratify>.
- (74) Tribelsky, M. I.; Flach, S.; Miroshnichenko, A. E.; Gorbach, A. V.; Kivshar, Y. S. Light scattering by a finite obstacle and Fano resonances. *Physical Review Letters* **2008**, *100*, 043903.
- (75) Miroshnichenko, A. E. Off-resonance field enhancement by spherical nanoshells. *Physical Review A* **2010**, *81*, 053818.
- (76) Messinger, B. J.; von Raben, K. U.; Chang, R. K.; Barber, P. W. Local fields at the surface of noble-metal microspheres. *Physical Review B* **1981**, *24*, 649–657.
- (77) Zuloaga, J.; Nordlander, P. On the energy shift between near-field and far-field peak intensities in localized plasmon systems. *Nano Letters* **2011**, *11*, 1280–1283.
- (78) Dubertret, B.; Calame, M.; Libchaber, A. J. Single-mismatch detection using gold-quenched fluorescent oligonucleotides. *Nature Biotechnology* **2001**, *19*, 365–370.
- (79) Schelm, S.; Smith, G. B. Internal electric field densities of metal nanoshells. *Journal of Physical Chemistry B* **2005**, *109*, 1689–1694.
- (80) Gersten, J.; Nitzan, A. Spectroscopic properties of molecules interacting with small dielectric particles. *Journal of Chemical Physics* **1981**, *75*, 1139–1152.
- (81) Moroz, A. Non-radiative decay of a dipole emitter close to a metallic nanoparticle: Importance of higher-order multipole contributions. *Optics Communications* **2010**, *283*, 2277–2287.

- (82) Moroz, A. Depolarization field of spheroidal particles. *Journal of the Optical Society of America B* **2009**, *26*, 517–527.

Graphical TOC Entry



Supporting information for:

The critical role of shell in enhanced fluorescence of metal-dielectric core-shell nanoparticles

Song Sun,^{*,†,‡,||} Ilia L. Rasskazov,^{*,¶,||} P. Scott Carney,[¶] Taiping Zhang,^{†,‡} and
Alexander Moroz^{*,§}

[†]*Microsystem and Terahertz Research Center, China Academy of Engineering Physics, No. 596, Yinhe Road, Shuangliu, Chengdu, 610200, China*

[‡]*Institute of Electronic Engineering, China Academy of Engineering Physics, Mianyang, 621999, China*

[¶]*The Institute of Optics, University of Rochester, Rochester, NY 14627, USA*

[§]*Wave-scattering.com*

^{||}*Contributed equally to this work*

E-mail: sunsong@mtrc.ac.cn; irasskaz@ur.rochester.edu; wavescattering@yahoo.com

1 Additional data on calculation methods

1.1 Benchmarking with the finite-element method

Our transfer matrix method^{?, ?} is an exact analytic solution of the Maxwell equations. The analytical methods from Sec. 2 have been implemented with the in-house developed Matlab code,[?] which has been used in simulations. Its Fortran version for decay rates has been since 2006 freely available from www.wave-scattering.com/codes.html. In order to disperse any

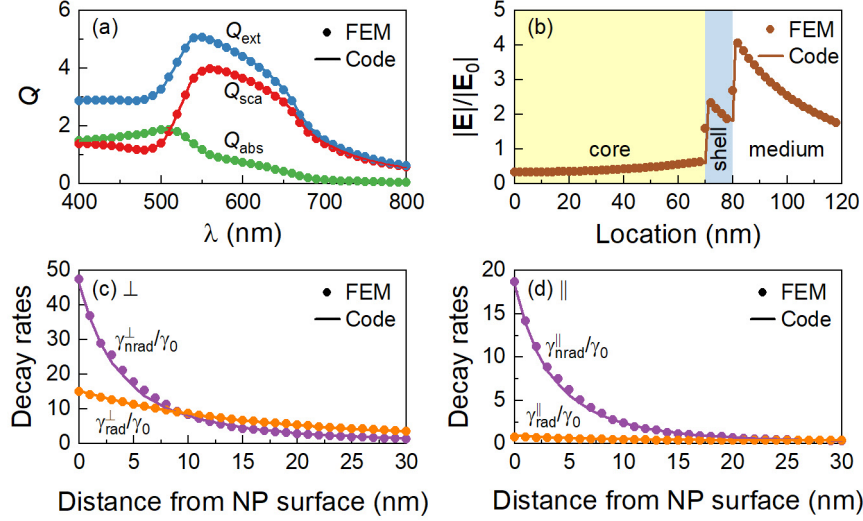


Figure S1: Benchmark results for Au@SiO₂ core-shell: (a) extinction, scattering and absorption spectra, (b) normalized electric field distributions under plane wave excitation, and fluorescence decay rates for (c) perpendicular and (d) parallel dipole orientation. Parameters are set as: core radius $r_c = 70$ nm, shell thickness $t_s = 10$ nm, shell refractive index $n_s = 1.45$ at wavelength $\lambda = 550$ nm. A single FEM simulation takes 2-3 hours for fine mesh on the HPC server with 128 CPU and 512 GB RAM used. In contrast, our transfer matrix code based on analytical solution of Maxwell equations runs few seconds on a regular workstation with 16 CPU and 64 GB RAM.

doubt on the validity of our method we have found it expedient to compare it against the finite element method (FEM) using COMSOL Multiphysics, for the case of Au@SiO₂ core-shell. In FEM simulations, the background field was set to be the plane wave during the excitation process and zero during the dipole emission process. The perfect matching layer (PML) surrounding the computational domain was used to absorb any unphysical reflections. The near field distribution can be probed anywhere in the computational domain, and the normalized fluorescence decay rates can be obtained straightforwardly using the scattering and absorption power quantities.^{???} The benchmark results are illustrated in Figure S1. It is clear that our code agrees with the FEM simulations. However our transfer matrix code, which was specifically designed for core-shell particles, is several orders of magnitude faster.

1.2 Finding optimal core-shell configurations

Figure S2 shows the example of $\eta_{\text{em}}/\eta_{\text{em};0}$ calculation in (r_c, t_s) parameter space for Au@SiO₂ core-shells at $\lambda_{\text{exc}} = \lambda_{\text{em}} = 642$ nm embedded in air (cf. Figures 4 and 5). A clear existence of an optimal core-shell configuration for gaining maximum fluorescence enhancement is observed. Noteworthy, the moderate deviations of r_c and t_s from optimally chosen values may yield in only slight decrease of the fluorescence enhancement factor.

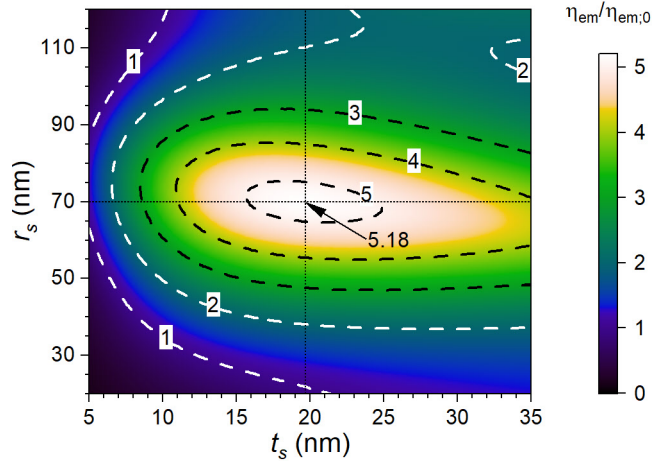


Figure S2: Fluorescence enhancement at $\lambda_{\text{exc}} = \lambda_{\text{em}} = 642$ nm for Au@SiO₂ core-shell nanoparticle embedded in air. The $\max(\eta_{\text{em}}/\eta_{\text{em};0}) = 5.18$ is observed for $r_c = 70$ nm and $t_s = 19.7$ nm which are shown with black horizontal and vertical dotted lines, correspondingly.

2 Additional data for fluorescence enhancement

2.1 Electric field enhancement at shell-medium interface

To elaborate the optimized results in Figures 2 and 3, below we discuss the effect of dielectric shell in manipulating various fluorescence parameters. For illustration purpose, Au@dielectric structure is considered, while the same conclusion can be extended to the Ag core cases. The emitter is assumed to be located at the hot spot of the shell surface for both perpendicular and parallel emitter dipole orientations. Under the plane wave excitation, it is well known that the presence of the dielectric shell red-shifts the LSPR[?] as shown

in Figure S3a, where the shell thickness t_s varies from 0 nm to 30 nm, and the shell refractive index $n_s = 1.45$ (SiO_2). The corresponding resonant peak position changes from 530 nm (homogeneous Au sphere) to 630 nm ($t_s = 30$ nm). The evolution of electric field distributions of the core-shell nanoparticle at different wavelengths ($\lambda = 530, 570, \dots, 690$ nm) are illustrated in Figure S3b–S3f, respectively. The electric field intensity increases at the core/shell interface with subsequent decrease inside the dielectric shell with increasing distance to the core.

At the LSPR of a homogeneous Au sphere at $\lambda = 530$ nm, the electric field intensity of the core-shell particles are generally below that of a homogeneous Au sphere, regardless of the shell thickness t_s , because the LSPR of core-shell particles is red shifted. With increasing distance from the shell, electric field intensity gradually decreases to the incident field intensity value. As λ increases, the electric field intensity at the shell-medium interface can achieve higher values than that at the same distance from Au surface of a homogeneous particle. In addition, the increment of the electric field at the shell-medium interface is more prominent for a larger t_s at a larger λ , since the electric field strength and the resonant wavelength are inter-correlated.

Figure S4a shows the corresponding electric field intensity at the shell-medium interface as a function of the shell thicknesses. It is found that the dielectric shell can slow the decrease of electric field at the shell-medium interface, in particular for a large wavelength. For illustration, Figure S4d compares the profiles of the electric fields at the shell-medium interface with those of Au sphere in the homogeneous medium at $\lambda = 690$ nm. It is obvious that the electric fields at the shell-medium interface decrease slower than that of the Au sphere in the homogeneous medium. The electric field at $t_s = 30$ nm drops only by 16.8% compared to that at $t_s = 0$ nm, whereas the electric field around Au sphere drops by 48.5% in the homogeneous medium at the 30 nm distance.

In Figure S4a, the highest electric field always occurs at $t_s = 0$ nm regardless of the wavelength. Such constraint can easily be broken by utilizing the dielectric shell with higher

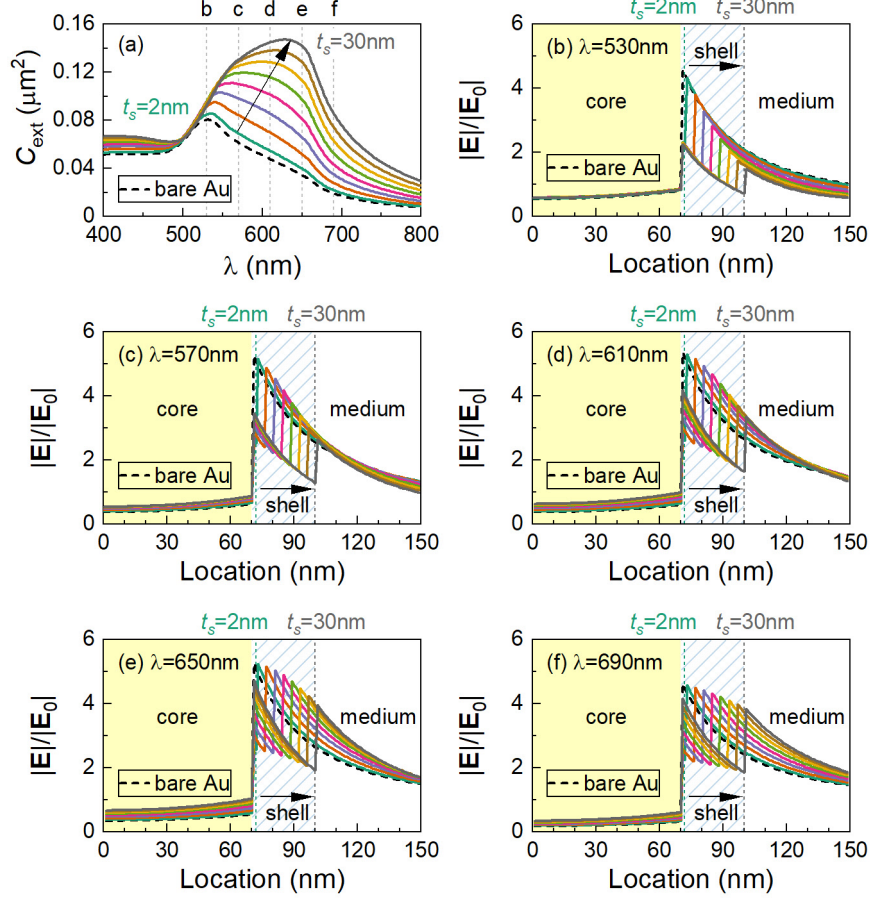


Figure S3: (a) Extinction spectra of core-shell nanoparticle with shell thicknesses from $t_s = 2 \text{ nm}$ to $t_s = 30 \text{ nm}$ with a 4 nm step. (b)-(f) Electric field enhancement at different wavelengths. Parameters are set as: core radius $r_c = 70 \text{ nm}$, shell refractive index $n_s = 1.45$. Black dashed lines show corresponding curves for bare Au nanoparticles.

refractive index. Figures S4b-c monitor the electric fields at the shell-medium interface with relatively larger shell refractive indices $n_s = 1.76$ (Al_2O_3) and $n_s = 2.00$ (ZnO), respectively. A high shell refractive index could boost the electric field at the shell-medium interface more effectively, leading to a larger electric field than that at $t_s = 0 \text{ nm}$, which in turn could further slow its decrease. Figures S4e-f confirm this point by comparing the profiles of the electric fields at the shell-medium interface with that of Au sphere in a homogeneous medium at $\lambda = 690 \text{ nm}$. The electric field decreases even more slower than that with $n_s = 1.45$ (see Figure S4e), i.e. the electric field at $t_s = 30 \text{ nm}$ drops by merely 1.4% compared to that at $t_s = 0 \text{ nm}$ for $n_s = 1.76$, and it even increases by 3.1% for $n_s = 2.00$.

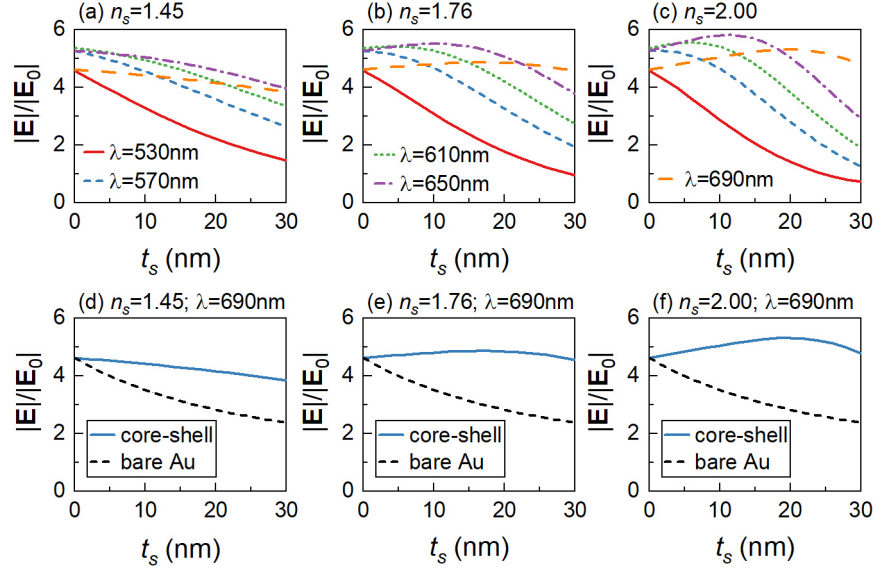


Figure S4: (a)-(c) Electric field intensity at the shell-medium interface as a function of shell thicknesses for shell refractive indices $n_s = 1.45$, 1.76 and 2.00 , respectively. (d)-(f) Comparison between electric field at shell-medium interface and that of Au sphere in homogeneous medium at wavelength $\lambda = 690$ nm. Au core radius is $r_c = 70$ nm in all cases. Dielectric shell with higher refractive index could boost electric field at shell-medium interface more effectively, and slow its decay even further.

The electric field at the shell-medium interface could be maintained at a high value even with a relatively thick dielectric shell. If the emitter is attached at the core-shell surface, it will experience a much higher fluorescence excitation rate than around a Au sphere at an equivalent distance. Combined with a decelerated decrease of electric field, a better balance between the fluorescence excitation rate and quantum yield can be achieved.

2.2 Radiative and non-radiative decay rates at shell-medium interface

The presence of the dielectric shell could not only manipulate the excited electric field distribution, but also has a remarkable influence on the dipole decay rates as governed by eq 2. Figures S5a–S5e and S5g–S5k show the radiative and non-radiative decay rates of a perpendicular-oriented emitter. The results confirm that the core-shell structure could significantly manipulate both the radiative and non-radiative decay rates at the shell-medium

interface, leading to the decelerated decrease as shown in Figure S5f and S5l, respectively. Again, the dipole decay rates at the shell-medium interface decrease slower at a larger wavelength, where the thicker dielectric shell has stronger influence.

Likewise, the decelerated decrease of the dipole decay rates at the shell-medium interface can be further manipulated by varying the refractive index of the dielectric shell. Figures S6a-c and S6g-i show dipole decay rates at the shell-medium interface for a *radially* oriented dipole emitter in the case of the shell refractive indices $n_s = 1.45$, 1.76 and 2.00 , respectively. The comparison of these quantities to those of the Au sphere in the homogeneous medium for $\lambda = 690$ nm are illustrated in Figure S6d-S6f and S6j-S6l, respectively. The results show that the dielectric shell with higher refractive index could further slow the decrease of both radiative and non-radiative decay components at the shell-medium interface. In particular, the highest radiative decay rates at the shell-medium interface with a shell thickness $t_s = 20$ nm and a shell refractive index $n_s = 1.76$ and 2.00 could easily exceed those for Au sphere. Note that both radiative and non-radiative decay rates could be enhanced at the shell-medium interface compared to those of the homogeneous Au sphere, because both the absorption and scattering efficiency of core-shell nanoparticle are larger than those of the homogeneous Au sphere.[?]

Figure S7 shows dipole decay rates at the shell-medium interface for a *parallel* oriented dipole emitter. Figures S7a-S7c and S7g-S7i show the radiative and nonradiative decay rates at the shell-medium interface for various shell refractive indices, and the comparisons between the core-shell structure and the Au sphere counterpart are illustrated in Figures S6d-S6f and S6j-S6l, respectively. Both radiative and nonradiative decay rates at the shell-medium interface are generally larger compared to those of the Au sphere. Note that the absolute magnitudes of the dipole decay rates for the parallel-oriented emitter is much smaller than those for the radially oriented emitter, which is consistent with the results in Figure 4 and with literature.^{???}

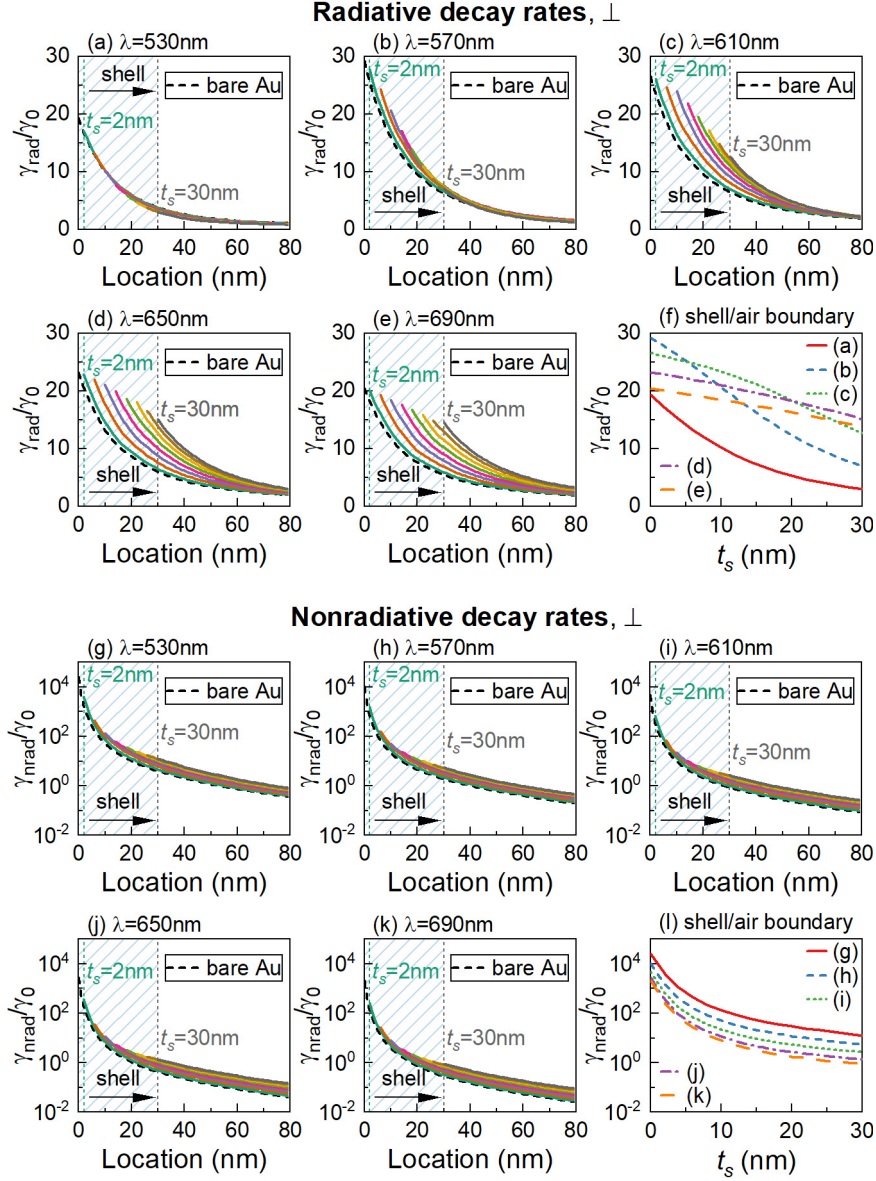


Figure S5: (a)-(e) Radiative and (g)-(k) non-radiative decay rates of radially oriented dipole emitter as a function of the distance from nanoparticle surface for various wavelengths. (f) Radiative and (l) non-radiative decay rates at the shell-medium interface, respectively. Au core radius is $r_c = 70$ nm in all cases. Core-shell structure could manipulate both radiative and non-radiative decay rates, leading to decelerated decrease at shell-medium interface.

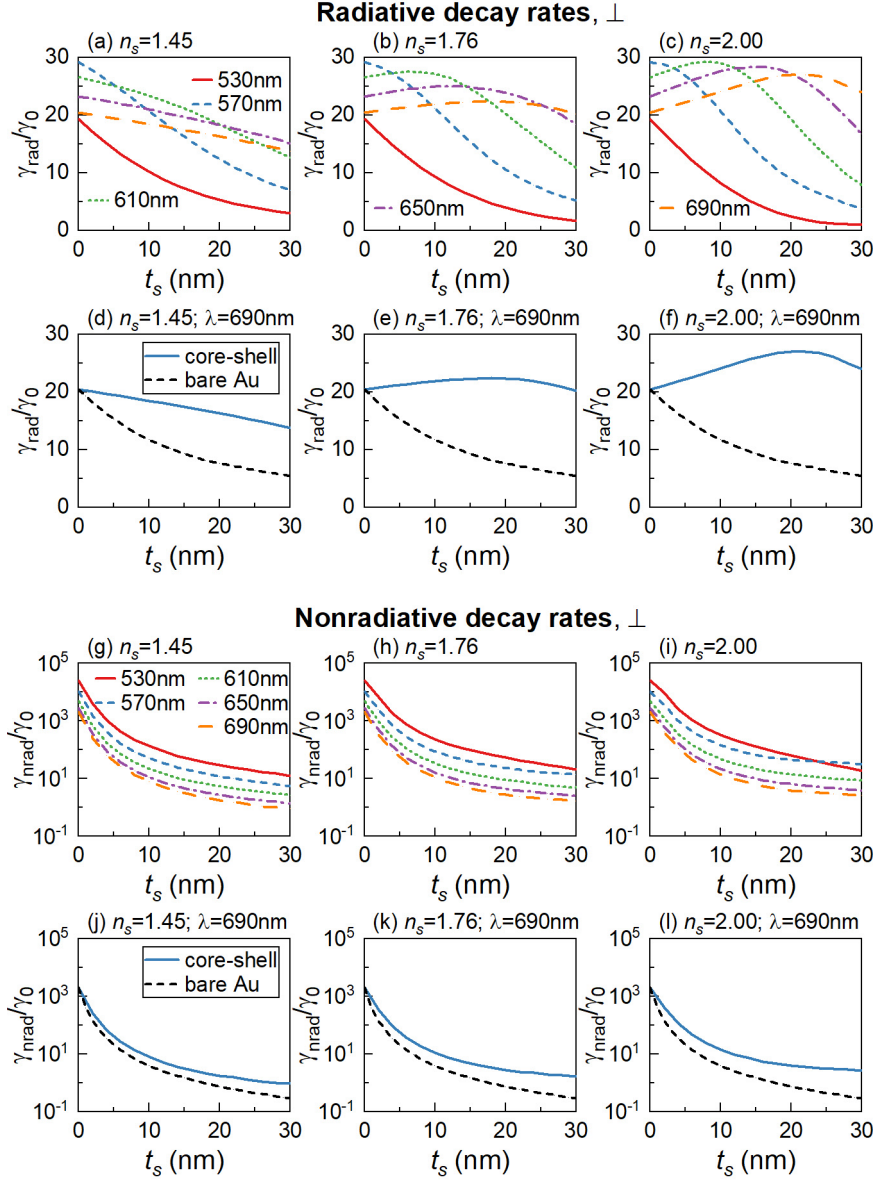


Figure S6: (a)-(c) Radiative and (g)-(i) non-radiative decay rates of perpendicular-oriented emitter at the shell-medium interface for shell refractive indices $n_s = 1.45, 1.76$ and 2.00 . Comparison of (d)-(f) radiative and (j)-(l) non-radiative decay rates at the shell-medium interface with those of Au sphere in homogeneous medium for $\lambda = 690$ nm. Au core radius is $r_c = 70$ nm in all cases. Dielectric shell with higher refractive index could improve both radiative and non-radiative decay rates at the shell-medium interface more effectively, and to slow their decrease even further.

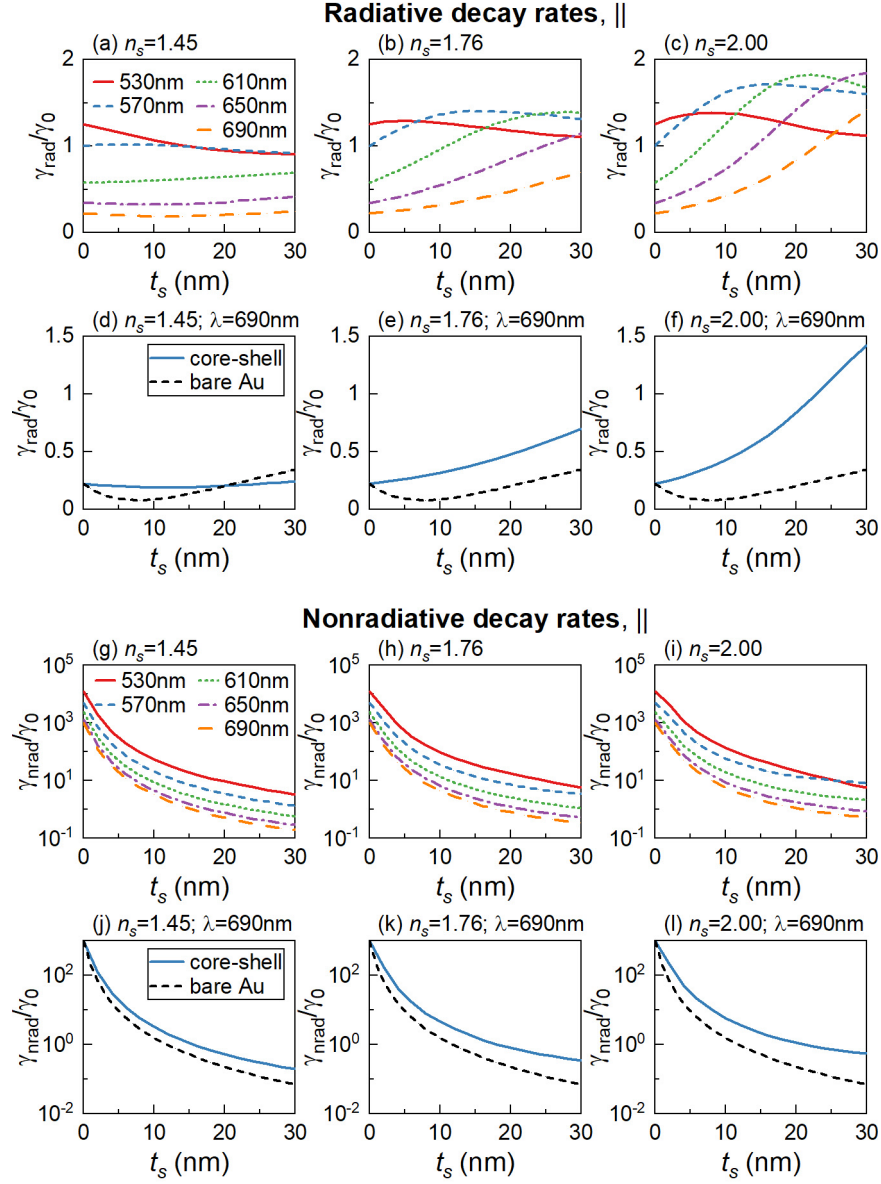


Figure S7: (a)-(c) Radiative and (g)-(i) nonradiative decay rates of parallel-oriented dipole emitter at the shell-medium interface for shell refractive indices $n_s = 1.45, 1.76$ and 2.00 . Comparison of (d)-(f) radiative and (j)-(l) nonradiative decay rates at the shell-medium interface with those of Au sphere for $\lambda = 690$ nm. Au core radius is $r_c = 70$ nm in all cases. Influence of dielectric shell on parallel-oriented dipole emitter is similar to that of radially oriented emitter.

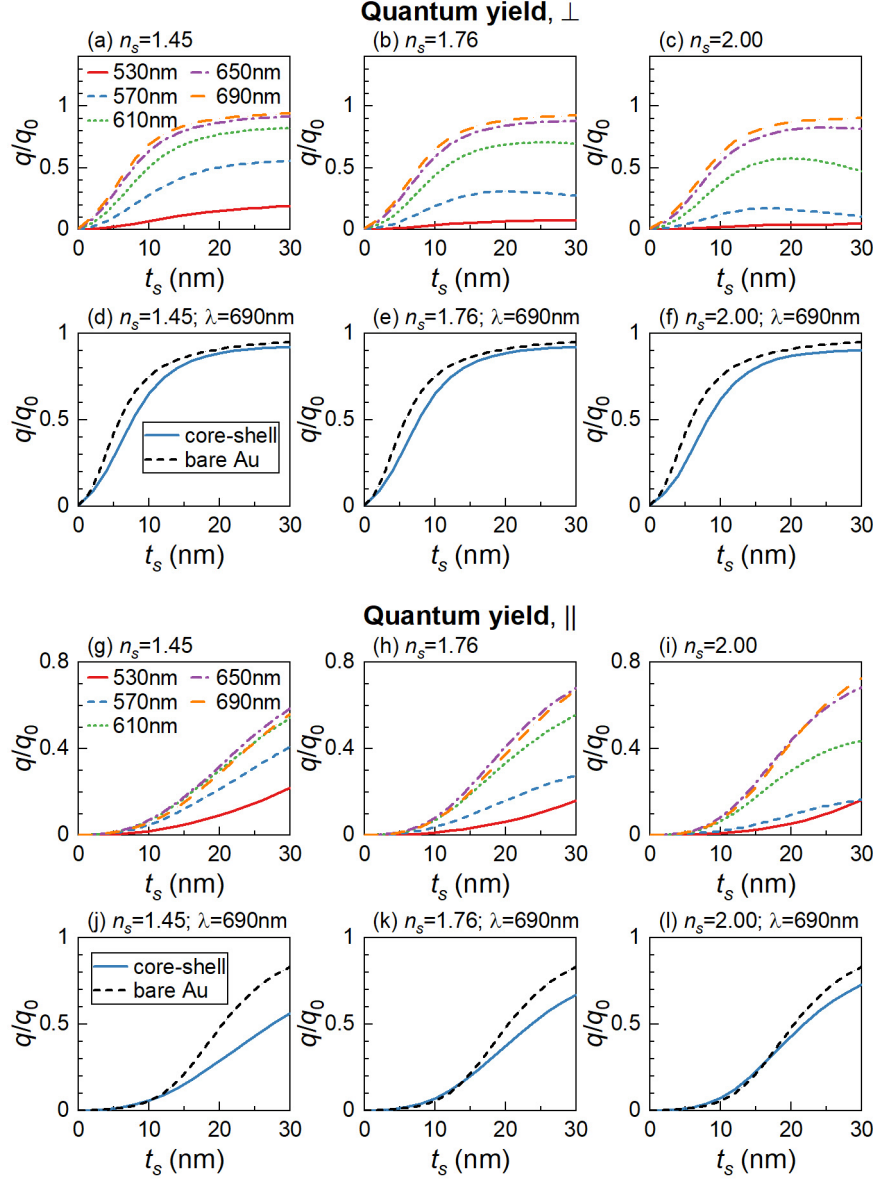


Figure S8: Quantum yields for (a)-(c) perpendicular-oriented and (g)-(i) parallel-oriented dipole emitters at the shell-medium interface for shell refractive indices $n_s = 1.45$, 1.76 and 2.00 . Comparison of quantum yields at the shell-medium interface with those around bare Au sphere for (d)-(f) perpendicular-oriented and (j)-(l) parallel-oriented emitters at $\lambda = 690$ nm. Au core radius is $r_c = 70$ nm in all cases. Core-shell particles exhibit similar quantum yields at the shell-medium interface compared to those around Au sphere at equivalent distances.

2.3 Quantum yield

Figures S8a–S8c show the quantum yields for the perpendicular-oriented emitter at the shell-medium interface at various wavelengths. The quantum yields are generally larger at

larger wavelength, because the radiative components are maintained at a comparable level regardless of the wavelength while the nonradiative decay rates are dramatically reduced at larger wavelength. In addition, the quantum yield increases as the shell thickness increases, because the radiative decay rates are relatively the same even for sufficiently thick shells, whereas the nonradiative decay rates decrease as the shell thickness increases. Figures S8d–S8f compare the quantum yields at the shell-medium interface with those around Au sphere in the homogeneous medium at $\lambda = 690$ nm. The quantum yields at the shell-medium interface are slightly smaller than that of the bare Au particle at the equivalent distance, because both the radiative and nonradiative decay components are enhanced at the shell-medium interface. Note that the quenching effect might still exist for a thin shell (i.e. $t_s < 5$ nm), which should be avoided in the practical experiments. The conclusion also holds valid for the parallel-oriented emitter, which are shown in Figures S8g–S8l. The profile of the quantum yield for the parallel-oriented emitter is different with that of the perpendicular-oriented emitter, which is attribute to the difference in the profile of radiative decay rates as shown in Figure S7. Note in passing that the comparison between core-shell particle and bare Au in Figure S8 is at the *same* wavelength, and the quantum yield of the core-shell particle is slightly smaller than that of bare Au. Whereas the comparison in Figure 5 in the main text is at the corresponding optimal conditions of the two configurations, where the optimal wavelength of the core-shell particle is larger than that of bare Au, and the resultant quantum yield of the core-shell structure is larger than that of bare Au.

2.4 Fluorescence enhancement

The ultimate fluorescence enhancement factor is obtained via multiplying the excitation rate and quantum yield. Figures S9a–S9c illustrate the fluorescence enhancement factors for the perpendicular-oriented emitter at the shell-medium interface at various wavelengths and shell refractive indices. In general, larger fluorescence enhancement factor is achieved at larger wavelength, due to the red-shift of the LSPR.

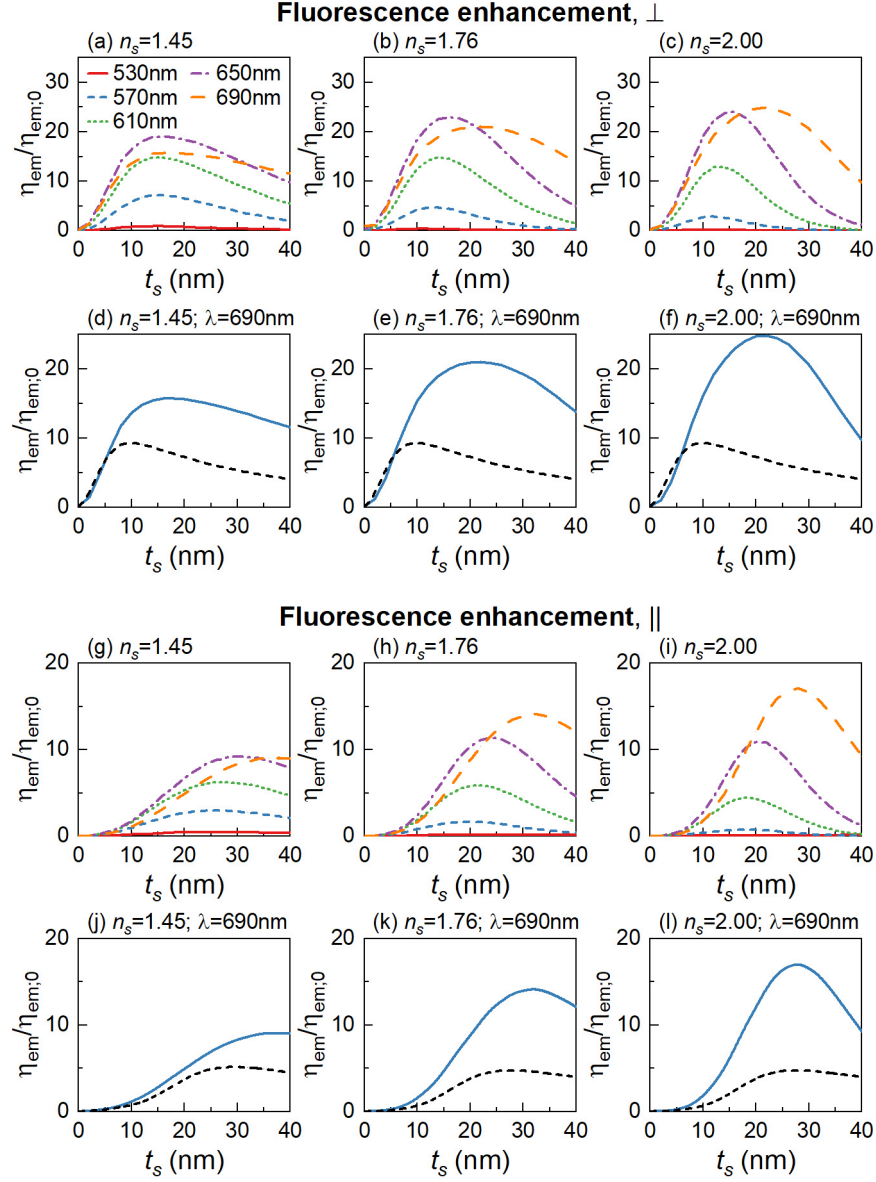


Figure S9: Fluorescence enhancement factors of (a)-(c) perpendicular-oriented and (g)-(i) parallel-oriented emitters at the shell-medium interface for shell refractive indices $n_s = 1.45$, 1.76 and 2.00. Comparison of fluorescence enhancement factors at the shell-medium interface with those around Au sphere in homogeneous medium for (d)-(f) perpendicular-oriented and j-(l) parallel-oriented emitters at $\lambda = 690$ nm. Au core radius is $r_c = 70$ nm in all cases. Core-shell nanoparticle could generate much larger enhancement factor at the shell-medium interface than those of bare Au particle at the comparable metal-dye distance.

Even larger fluorescence enhancement factor could be achieved by using a higher refractive index shell, which are attributed to its stronger capability in manipulating the decrease of excited electric fields and dipole decay rates. Figures S9d–S9f compares the fluorescence enhancement factors at the shell-medium interface with those around Au sphere in the homogeneous medium at $\lambda = 690$ nm. The core-shell nanoparticle could generate a much larger fluorescence enhancement factor at the shell-medium interface than that of the bare Au nanoparticle. On top of that, the maximum enhancement factors of the core-shell configurations appear at much longer distances than that of the bare Au particle, due to the decelerated decrease of electric field and dipole decay rates at the shell-medium interface. Similar results can also be obtained for the parallel-oriented emitter as shown in Figure S9g–S9l. These findings are consistent with the optimizations results in Figures 2 and 3.

3 Quasi-static formulas

The Gersten and Nitzan (GN) quasi-static approximation for determining decay rates,[?] which makes use of particle multipolar polarizabilities, α_ℓ , has been known to provide a very good approximation of radiative and nonradiative decay rates in the case of small homogeneous particles.[?] A dipolar polarizability of a core-shell particle with the account of dynamic depolarization and radiative correction[?] can be expressed as (cf. Eq.(23) in Ref. ?),

$$\alpha_1 = \frac{1}{3} r_2^3 \frac{(\varepsilon_2 - \varepsilon_h)[\varepsilon_1 q_1 - \varepsilon_2(q_1 - 1)]r_2^3 - (\varepsilon_1 - \varepsilon_2)[\varepsilon_2(q_2 - 1) - \varepsilon_h q_2]r_1^3}{[\varepsilon_1 q_1 - \varepsilon_2(q_1 - 1)][\varepsilon_2 q_2 - \varepsilon_h(q_2 - 1)]r_2^3 - (\varepsilon_1 - \varepsilon_2)(\varepsilon_2 - \varepsilon_h)q_2(q_2 - 1)r_1^3}, \quad (1)$$

where

$$q_j := \frac{1}{3} - \frac{1}{3} x_j^2 - i \frac{2}{9} x_j^3,$$

$x_j = kr_j$, and the respective r_1 and r_2 are the radii of the inner and outer surfaces. In the case of an improved modified long wavelength approximation (IMLWA),

$$q_j := \frac{1}{3} - \frac{1}{3} x_j^2 \left(1 - \frac{2\beta}{5} \right) - i \frac{2}{9} x_j^3, \quad (2)$$

where β is a dimensionless fitting parameter to account for a spatially inhomogeneous polarization,[?]

$$\mathbf{P} \rightarrow (1 + \beta k^2 r^2 \sin^2 \theta) \mathbf{P}, \quad (3)$$

the choice of $\beta = 1$ in eq 2 enabled rather precise description of the scattering properties of core-shell particles.[?]

To accurately describe multipole polarizabilities, we have employed an effective sphere dielectric constant, $\bar{\varepsilon}$:

$$\bar{\varepsilon} = \frac{1 + 2\alpha_1}{1 - \alpha_1}, \quad (4)$$

where α_1 is determined by eq 1. Substitution of $\bar{\varepsilon}$ into GN approximation[?] didn't result in any significant improvement, as shown in Figure 6.